Waveform inversion for localized seismic structure and an application to D structure beneath the Pacific

Kenji Kawai, Robert J. Geller

JOURNAL OF GEOPHYSICAL RESEARCH, VOL. 115, B01305, doi:10.1029/2009JB006503, 2010

Waveform inversion for localized seismic structure and an application to D″ structure beneath the Pacific

Kenji Kawai[1,2] and Robert J. Geller[3]

Received 1 April 2009; revised 22 September 2009; accepted 16 October 2009; published 29 January 2010.

[1] In order to extract more information on localized seismic structure from observed seismic data, we have developed and applied a new method of waveform inversion. The calculation of synthetic seismograms and their partial derivatives is the key steps in such an inversion. We formulate the inverse problem of waveform inversion for localized structure, computing partial derivatives for the 1-D and 3-D anisotropic elastic moduli at particular depth or at points in space. Our method does not use any great circle approximations in computing the synthetics and their partial derivatives. In this study we invert for the vertical dependence of the shear velocity in the lowermost mantle beneath the Pacific using the transverse component of broadband waveforms for the period range 8–200 s. We find 1%–1.5% velocity decreases and increases in the zones from 400 to 500 km and from 300 to 400 km above the core-mantle boundary (CMB), respectively. In addition, we find 0.5%–1% velocity increases and decreases in the zones from 100 to 200 km and from 0 to 100 km above the CMB, respectively. This is interpreted as evidence for phase transitions between perovskite and postperovskite (although a chemical stratification model cannot be excluded).

Citation: Kawai, K., and R. J. Geller (2010), Waveform inversion for localized seismic structure and an application to D″ structure beneath the Pacific, *J. Geophys. Res.*, *115*, B01305, doi:10.1029/2009JB006503.

1. Introduction

[2] There have been many waveform inversion studies of global upper mantle structure using surface waves [e.g., *Woodhouse and Dziewonski*, 1984] and of global whole mantle structure using both body and surface waves [e.g., *Li and Romanowicz*, 1996; *Megnin and Romanowicz*, 2000]. Almost all such studies used approximations such as the path average approximation or a nonlinear asymptotic normal mode approach [*Li and Romanowicz*, 1995] in computing synthetic seismograms in order to reduce computational requirements. Recently, as efficient methods for computing synthetic seismograms and their partial derivatives have been developed, waveform inversion for global upper mantle structure [*Hara and Geller*, 2000; *Hara*, 2004] and for global whole mantle structure [*Takeuchi*, 2007] has been conducted without using such approximations.

[3] On the other hand, there have been relatively few studies using body wave waveform inversion to determine localized structure in the Earth's deep interior, although waveform inversion for local structure of upper mantle using surface waves has been conducted [e.g., *Montagner*, 1986; *Nolet*, 1990]. Although long-period free oscillations provide information on deep structure, they can resolve only long wavelengths and are not ideal for studies of deep structure. It is desirable to use body waves, whose dominant period and wavelength is shorter than that of surface waves, to investigate localized structure in the Earth's deep interior. It is therefore necessary to develop efficient methods for computation of body wave synthetic seismograms and their partial derivatives.

[4] Almost all previous studies of local structure in the Earth's deep interior using body wave waveforms have been conducted using forward modeling in which the Earth model is perturbed by trial and error to improve the fit between the observed and synthetic waveforms. Such forward modeling studies have contributed greatly to understanding geodynamics [e.g., *Lay and Helmberger*, 1983; *Grand and Helmberger*, 1984; *Tajima and Grand*, 1998], but there are several inherent problems. First, the methods for computing the synthetics use some approximations (e.g., modal summation, reflectivity, generalized ray theory). Second, objectivity is lacking, as the fit between data and synthetics is evaluated qualitatively, not quantitatively. To further improve our knowledge of Earth structure, it is desirable to develop new methods for quantitative and objective waveform inversion of body wave data for localized structure in the Earth's deep interior.

[5] The regions which can be investigated are restricted in practice because of the inhomogeneous distribution of sources and receivers. This is why localized parameteriza-

[1]Department of Earth and Planetary Sciences, Tokyo Institute of Technology, Tokyo, Japan.
[2]Also at Institut de Physique du Globe de Paris, Paris, France.
[3]Department of Earth and Planetary Science, Graduate School of Science, University of Tokyo, Tokyo, Japan.

0148-0227/10/2009JB006503$09.00

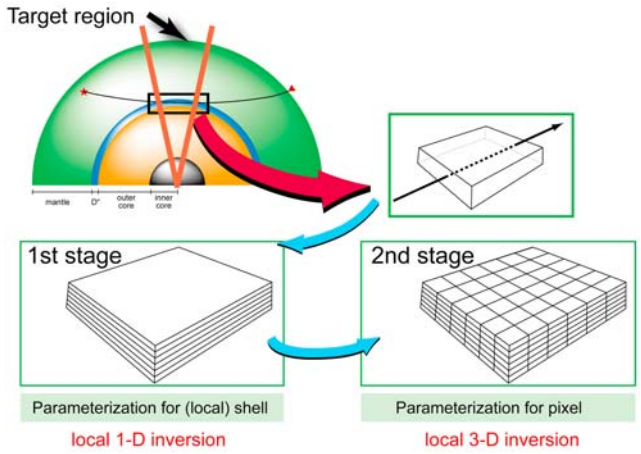

Figure 1. A possible strategy for waveform inversion for localized structure in the Earth's deep interior. Zeroth stage, determining target regions which are well sampled by waveforms excited in regions where earthquakes occur frequently and observed by dense receiver networks such as arrays; first stage, conducting waveform inversion for 1-D (vertically heterogeneous) local structure; second stage, inverting for 3-D local structure parameterized as voxel structure. In order to conduct waveform inversion for local structure, it is necessary to be able to efficiently compute partial derivatives for (local) shell and voxel perturbations.

tion (which can focus on only well-constrained regions) is preferable to the use of global basis functions (such as spherical harmonics), which uniformly models all structure, regardless of whether or not the data exist to provide constraints.

2. Formulation of Inverse Problem for Localized Structure

[6] In order to conduct inversion of body wave waveforms for localized Earth structure, several technical developments are necessary (Figure 1). *Kawai et al.* [2006] presented accurate and efficient methods for computing synthetic seismograms in a spherically symmetric, transversely isotropic, Earth model using the direct solution method (DSM) [*Geller and Ohminato*, 1994; *Geller and Takeuchi*, 1995]. These synthetics were recently used in waveform inversion for the local laterally homogeneous structure of D″ beneath Central America [*Kawai et al.*, 2007a, hereafter KTGF07], beneath the Arctic [*Kawai et al.*, 2007b], beneath the western Pacific [*Konishi et al.*, 2009], and beneath northern Asia [*Kawai et al.*, 2009]. We summarize our techniques for waveform inversion below, discussing in more detail those portions of our techniques which have not been presented in other publications.

2.1. Computation of Partial Derivatives

[7] We use the methods of *Geller and Hara* [1993] to compute the partial derivatives (Figure 2). We express the i component of the displacement for the kth earthquake at the point $\mathbf{r}$ as $u_i^{(k)}(\mathbf{r})$ and the i component of the back-propagated displacement at $\mathbf{r}$ excited by a point force in the j-direction at the pth station as $\eta_{ij}^{(p)}(\mathbf{r})$. Note that $\mathbf{r}$ will, in general, be a point in the Earth's interior.

[8] The partial derivatives are expressed as follows:

$$\left\{\frac{\partial u_i^{(k)}[\mathbf{r}^{(p)}]}{\partial m_l}\right\}^* = \int_V (\omega^*)^2 \left[u_j^{(k)}\right]^* \left[\rho^{(l)}\right]^* \eta_{ji}^{(p)} dV - \int_V \left[u_{j,q}^{(k)}\right]^* \left[C_{jqrs}^{(l)}\right]^* \eta_{ri,s}^{(p)} dV, \quad (1)$$

where ρ and C_{ijkl} are the density and elastic constants, respectively (see *Geller and Hara* [1993] for details). Although we can use equation (1) to obtain partial derivatives for arbitrary perturbations to the starting model, we focus here on voxel and (local) shell perturbations.

2.1.1. Voxel Perturbation

[9] We use a δ function as the spatial dependence of the model parameters in computation of partial derivatives for a voxel perturbation, $\rho^{(l)} = \delta\rho\delta(\mathbf{r} - \mathbf{r_0})$ or $C_{ijpq}^{(l)} = \delta C_{ijpq}$

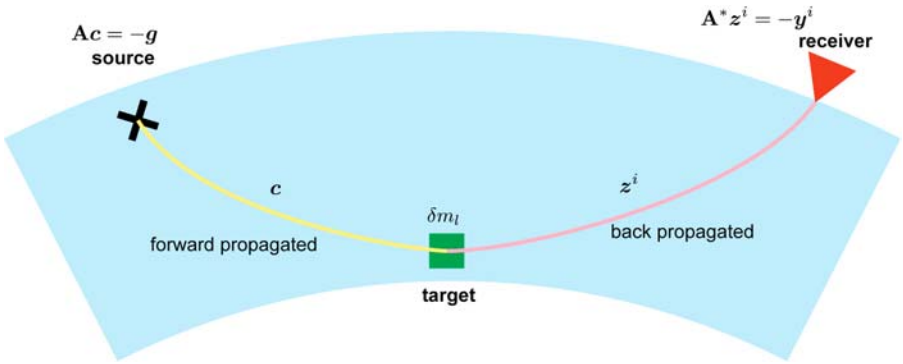

Figure 2. A schematic explanation of the partial derivatives, which are obtained by cross-correlation of functionals of the synthetics and functionals of the back-propagated synthetics. $\mathbf{A} \equiv \omega^2\mathbf{T} - \mathbf{H}$, where $\mathbf{T}$ and $\mathbf{H}$ are mass and stiffness matrices, respectively. The terms $\mathbf{c}$ and $\mathbf{z}^i$ are forward propagated wavefield and back-propagated wavefield excited by the ith direction point force, respectively. The terms $\mathbf{g}$ and $\mathbf{y}^i$ are the source excitation vector and the ith point force excitation vector, respectively. The term m_l is the lth model parameter. For a point perturbation the spatial dependence of the model parameters is given by a delta function, $\delta(\mathbf{r} - \mathbf{r}_0)$. For this case the partial derivatives can be obtained by evaluating the cross correlation of the kernels for the forward propagated and back-propagated waveforms at the particular point where the model is perturbed [*Geller and Hara*, 1993].

$\delta(\mathbf{r} - \mathbf{r_0})$. As the perturbation to the elastic parameters is expressed as $C^{(l)}_{ijpq}$, we can easily formulate the partial derivatives for general anisotropy and for the anelastic parameter Q. In Appendix A we present explicit expressions for the kernels of the partial derivatives with respect to the elastic constants for the transversely isotropic case. In this paper, we use these expressions to compute sensitivity in section 4.

2.1.2. (Local) Shell Perturbation

[10] In many cases the data are insufficient to invert for 3-D structure. In that case we will use a laterally homogeneous model appropriate for the study region. We may also want to first invert for a laterally homogeneous model and then use the localized 1-D model as the starting model for a localized 3-D inversion, as shown in Figure 1. The partial derivatives for spherically symmetric structure are as follows:

$$\left\{\frac{\partial u_i^{(k)}[\mathbf{r}^{(p)}]}{\partial m_l}\right\}^* = \int_V (\omega^*)^2 \left[u_j^{(k)}\right]^* \left[\rho^{(l)}\right]^* \eta_j^{i(p)} dV - \int_V \left[u_{j,q}^{(k)}\right]^* \left[C_{jqrs}^{(l)}\right]^* \eta_{r,s}^{i(p)} dV = (\omega^*)^2 \mathcal{T}^{i(l)} - \mathcal{H}^{i(l)}, \tag{2}$$

where u_i is the i component of the displacement and $\eta_i^{j(p)}$ is the i component of the back-propagated displacement excited by a point force in the j direction at the pth station. Spherically symmetric structure is represented as $\rho^{(l)} = \delta\rho^{(l)}\Psi(\mathbf{r})$ and $C^{(l)}_{jqrs} = \delta C^{(l)}_{jqrs}\,\Psi(\mathbf{r})$, where $\Psi(\mathbf{r}) = \psi(r)Y_{00}(\theta, \phi) = \psi(r)/\sqrt{4\pi}$, and the terms in the last line of equation (2) are written as follows:

$$\mathcal{T}^{i(l)} = \int_V \left[u_j^{(k)}\right]^* \delta\rho^* \Psi(\mathbf{r}) \left[\eta_j^{i(p)}\right] dV = \frac{1}{\sqrt{4\pi}} \int_V \left[u_j^{(k)}\right]^* \delta\rho^* \psi(r) \left[\eta_j^{i(p)}\right] dV = \frac{1}{\sqrt{4\pi}} \mathcal{T}^{i(l)}_{nt',mt} \tag{3}$$

$$\mathcal{H}^{i(l)} = \int_V \left[u_{j,q}^{(k)}\right]^* \delta C^*_{jqrs} \Psi(\mathbf{r}) \left[\eta_{r,s}^{i(p)}\right] dV = \frac{1}{\sqrt{4\pi}} \int_V \left[u_{j,q}^{(k)}\right]^* \delta C^*_{jqrs} \psi(r) \left[\eta_{r,s}^{i(p)}\right] dV = \frac{1}{\sqrt{4\pi}} \mathcal{H}^{i(l)}_{nt',mt}, \tag{4}$$

where n and m are pointers for the radial trial functions (we use linear splines in this study), and t and t' are indices for the polarization of the trial functions (see below). In discussing the partial derivatives, it is useful to introduce the commonly used functions $U(r)$, $V(r)$, and $W(r)$, which give the depth dependence of the spherical harmonic components of the displacement,

$$\mathbf{u}(r, \theta, \phi) = \sum_{lm} U_{lm}(r)\mathbf{S}^1_{lm}(\theta, \phi) + V_{lm}(r)\mathbf{S}^2_{lm}(\theta, \phi) + W_{lm}(r)\mathbf{T}_{lm}(\theta, \phi), \tag{5}$$

where

$$U_{lm}(r) = \sum_k U_1(r_k)X_k(r), \quad V_{lm}(r) = \sum_k U_2(r_k)X_k(r), \quad W_{lm}(r) = \sum_k U_3(r_k)X_k(r). \tag{6}$$

[11] The indices t and t' (introduced above) are 1 for $\mathbf{S}^1_{lm}$, 2 for $\mathbf{S}^2_{lm}$, and 3 for $\mathbf{T}_{lm}$. $X_k(r)$ specify the vector spherical harmonic: the vertically dependent parts of the trial functions (typically linear splines).

2.1.3. Partial Derivatives for Isotropy and Transverse Isotropy

[12] The expressions in equations (3) and (4) are general and can be applied to any laterally homogeneous structure (e.g., including anelastic attenuation). However, inversion for laterally homogeneous general anisotropy is unrealistic because of the trade-offs that are involved. The most general anisotropic structure for which it is appropriate to invert for laterally homogeneous structure may be transverse isotropy with a vertical symmetry axis (TI). We restrict the following discussion to a TI medium. Note, however, that the methods of this study can be extended to the general anisotropic case in a straightforward fashion.

[13] We define the following intermediate integrals:

$$\begin{aligned}
P^{i(0)}_{n,m} &= \int dr\delta\rho^* r^2 U_n^{(f)*}\psi(r)U_m^{i(b)} & P^{i(1)}_{n,m} &= \int dr\delta C^* r^2 \frac{dU_n^{(f)*}}{dr}\psi(r)\frac{dU_m^{i(b)}}{dr},\\
P^{i(2)}_{n,m} &= \int dr\delta L^* r^2 \frac{dU_n^{(f)*}}{dr}\psi(r)\frac{dU_m^{i(b)}}{dr} & P^{i(3)}_{n,m} &= \int dr\delta F^* r U_n^{(f)*}\psi(r)\frac{dU_m^{i(b)}}{dr},\\
P^{i(3')}_{n,m} &= \int dr\delta F^* r \frac{dU_n^{(f)*}}{dr}\psi(r)U_m^{i(b)} & P^{i(4)}_{n,m} &= \int dr\delta L^* r \frac{dU_n^{(f)*}}{dr}\psi(r)U_m^{i(b)},\\
P^{i(4')}_{n,m} &= \int dr\delta L^* r U_n^{(f)*}\psi(r)\frac{dU_m^{i(b)}}{dr} & P^{i(5)}_{n,m} &= \int dr\delta A^* U_n^{(f)*}\psi(r)U_m^{i(b)},\\
P^{i(6)}_{n,m} &= \int dr\delta L^* U_n^{(f)*}\psi(r)U_m^{i(b)} & P^{i(7)}_{n,m} &= \int dr\delta N^* U_n^{(f)*}\psi(r)U_m^{i(b)},
\end{aligned} \tag{7}$$

where A, C, F, L, and N are the five independent elastic constants for TI as defined by *Love* [1927], and $U^{(f)}$ and $U^{i(b)}$ indicate the forward wavefield and the back-propagated wavefield for a point force source at the receiver in the i-direction, respectively.

[14] Using the above intermediate expressions, the matrix elements for the partial derivatives for the spheroidal case ($t = 1$ or $t = 2$) are

$$\mathcal{T}^{i(l)}_{n1,m1} = \mathcal{T}^{i(l)}_{n2,m2} = P^{i(0)}_{n,m}, \quad \mathcal{T}^{i(l)}_{n1,m2} = \mathcal{T}^{i(l)}_{n2,m1} = 0 \tag{8}$$

and

$$\begin{aligned}
\mathcal{H}^{i(l)}_{n1,m1} &= P^{i(1)}_{n,m} + 2\left(P^{i(3)}_{n,m} + P^{i(3')}_{n,m}\right) + 4P^{i(5)}_{n,m} + \mathcal{L}^2 P^{i(6)}_{n,m} - 4P^{i(7)}_{n,m},\\
\mathcal{H}^{i(l)}_{n2,m2} &= P^{i(2)}_{n,m} - \left(P^{i(4)}_{n,m} + P^{i(4')}_{n,m}\right) + \mathcal{L}^2 P^{i(5)}_{n,m} + P^{i(6)}_{n,m} - 2P^{i(7)}_{n,m},\\
\mathcal{H}^{i(l)}_{n1,m2} &= -\mathcal{L}\left(P^{i(3')}_{n,m} - P^{i(4')}_{n,m} + 2P^{i(5)}_{n,m} + P^{i(6)}_{n,m} - 2P^{i(7)}_{n,m}\right),\\
\mathcal{H}^{i(l)}_{n2,m1} &= -\mathcal{L}\left(P^{i(3)}_{n,m} - P^{i(4)}_{n,m} + 2P^{i(5)}_{n,m} + P^{i(6)}_{n,m} - 2P^{i(7)}_{n,m}\right),
\end{aligned} \tag{9}$$

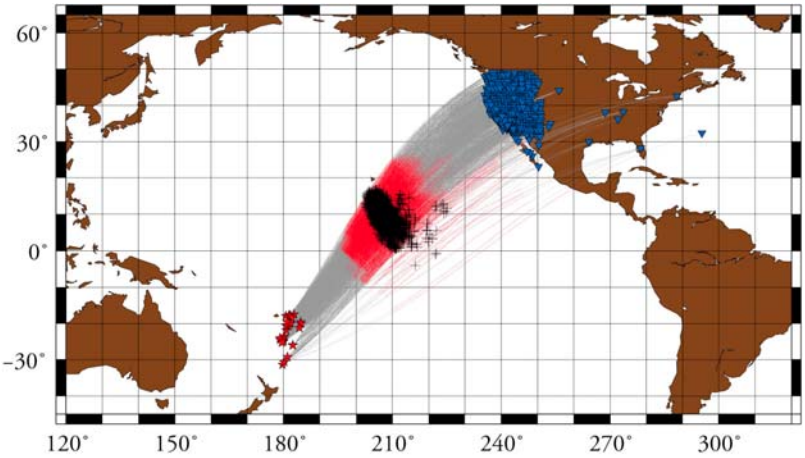

Figure 3. Event-receiver geometry, with great circle raypaths. The ray-paths are shown to indicate the coverage, but note that we do not use a ray theoretical approximation. The portions of the great circles which sample D″ are shown in red. Blue inverted triangles and red stars show the sites of stations used in our study and earthquakes studied, respectively. Pluses show the bottoming point of each ray, except that no pluses are shown for diffracted waves.

where $\mathcal{L}^2 = l\ (l+1)$. The explicit form of the matrix elements for the toroidal case ($t = 3$) is

$$\begin{aligned} \mathcal{T}^{i(l)}_{n3,m3} &= P^{i(0)}_{n,m} \\ \mathcal{H}^{i(l)}_{n3,m3} &= P^{i(2)}_{n,m} - P^{i(4)}_{n,m} - P^{i(4')}_{n,m} + P^{i(6)}_{n,m} + \left(\mathcal{L}^2 - 2\right)P^{i(7)}_{n,m}. \end{aligned} \tag{10}$$

If partial derivatives for isotropic media are required, we can easily obtain them by the following substitutions: (A, C, F, L, N) $\rightarrow$ ($\lambda + 2\mu$, $\lambda + 2\mu$, λ, μ, μ).

2.1.4. Locally Cartesian Derivatives

[15] The locally Cartesian derivatives of a vector u_i in spherical coordinates are given by

$$\begin{bmatrix} u_{r,r} & u_{r,\theta} & u_{r,\phi} \\ u_{\theta,r} & u_{\theta,\theta} & u_{\theta,\phi} \\ u_{\phi,r} & u_{\phi,\theta} & u_{\phi,\phi} \end{bmatrix} = \begin{bmatrix} \dfrac{\partial u_r}{\partial r} & \dfrac{1}{r}\dfrac{\partial u_r}{\partial \theta} - \dfrac{u_\theta}{r} & \dfrac{1}{r\sin\theta}\dfrac{\partial u_r}{\partial \phi} - \dfrac{u_\phi}{r} \\ \dfrac{\partial u_\theta}{\partial r} & \dfrac{1}{r}\dfrac{\partial u_\theta}{\partial \theta} + \dfrac{u_r}{r} & \dfrac{1}{r\sin\theta}\dfrac{\partial u_\theta}{\partial \phi} - \dfrac{u_\phi \cot\theta}{r} \\ \dfrac{\partial u_\phi}{\partial r} & \dfrac{1}{r}\dfrac{\partial u_\phi}{\partial \theta} & \dfrac{1}{r\sin\theta}\dfrac{\partial u_\phi}{\partial \phi} + \dfrac{u_r}{r} + \dfrac{u_\theta \cot\theta}{r} \end{bmatrix}. \tag{11}$$

Similarly, the locally Cartesian gradient of a scalar A for spherical coordinates is given by

$$\left(A_{,r},\ A_{,\theta},\ A_{,\phi}\right) = \left(\frac{\partial A}{\partial r}, \frac{1}{r}\frac{\partial A}{\partial \theta}, \frac{1}{r\sin\theta}\frac{\partial A}{\partial \phi}\right). \tag{12}$$

2.1.5. Synthetic Seismograms and Partial Derivatives for Arbitrary Depths

[16] Recently, seafloor and borehole observatories have been deployed [*Suetsugu et al.*, 2005; *Sutherland et al.*, 2004]. As such observatories are not deployed on the Earth's surface, it is necessary to be able to compute synthetic seismograms for arbitrary receiver depths in order to fully utilize waveforms from such observatories. As discussed above, it is also necessary to be able to accurately compute partial derivatives of the synthetics with respect to radius at arbitrary depths in order to conduct waveform inversion for localized structure.

[17] The computation using the DSM operators for a laterally homogeneous model [*Kawai et al.*, 2006] gives displacements at the nodes of the computational grid. The derivatives with respect to r cannot be obtained analytically. We therefore use three-point interpolation to compute the wavefield and its partials at arbitrary depths.

[18] On the other hand, when we differentiate the displacement field, we can easily obtain partials with respect to θ or ϕ analytically because the lateral dependence of the wavefield is parameterized in terms of spherically harmonics. The software to compute synthetics for arbitrary depths have been used by *Suetsugu et al.* [2005].

3. Inversion of Observed Data for D″ Structure Beneath the Pacific

[19] In section 2, we outlined our methods for inferring localized seismic structure. In this section, we apply these methods to observed data. The target of the inversion is the D″ layer beneath the Pacific. Many tomographic studies [e.g., *Megnin and Romanowicz*, 2000; *Grand*, 2002] have suggested that there is a large-scale, low-velocity region beneath the Pacific. It is controversial whether this is due to temperature variation, chemical heterogeneity, or both. Given that the outer core is primarily liquid iron, various chemical reactions and heterogeneous distributions of elements are expected at the base of the mantle. Also, the phase transition from perovskite (pv) to postperovskite (ppv) occurs under the pressure-temperature conditions at the depth of the lowermost mantle [*Murakami et al.*, 2004]. Thus, determining the detailed seismological structure of the lowermost mantle can provide clues to understanding the origin of this large low-velocity region.

[20] The recent deployment of the USArray has improved our resolution of this region by making it possible to use deep sources under Tonga-Fiji (Figure 3), but almost all data

Table 1. Earthquakes Used in This Study

Event	Date[a]	Centroid Time (UT)	Depth (km)	Latitude	Longitude	M_w	Half Duration (s)
050227	2005/02/27	0454:54.4	580.9	−17.66°	−178.52°	5.7	1.7
050319	2005/03/19	1734:50.3	609.2	−21.88°	−179.27°	6.3	3.4
050520	2005/05/20	1240:46.6	573.3	−24.43°	179.04°	5.9	2.3
050607	2005/06/07	0422:04.0	326.1	−29.20°	−178.90°	5.7	1.8
050806	2005/08/06	0956:18.2	217.7	−19.60°	−175.35°	6.0	2.3
050901	2005/09/01	1122:14.9	542.8	−24.55°	179.92°	5.6	1.4
050912	2005/09/12	2115:09.4	415.7	−17.51°	−177.09°	5.7	1.8
051125	2005/11/25	0930:02.0	180.7	−25.88°	−177.46°	5.5	1.5
060202	2006/02/02	1248:48.1	611.6	−17.77°	−178.13°	6.7	5.5
060224	2006/02/24	1415:49.0	640.9	−17.94°	−179.42°	6.1	2.6
060226	2006/02/26	0308:31.8	553.9	−23.59°	−179.82°	6.4	3.8
060305	2006/03/05	0808:01.6	213.9	−20.09°	−175.22°	6.1	2.7
060320	2006/03/20	1738:11.0	550.7	−23.85°	179.97°	5.8	1.8
060414	2006/04/14	0330:22.8	166.8	−25.99°	−177.44°	5.5	1.4
060506	2006/05/06	0229:33.2	528.2	−25.03°	179.90°	5.6	1.5
060602	2006/06/02	0731:38.0	584.6	−20.77°	−178.54°	6.0	2.4
060611	2006/06/11	0546:03.2	670.3	−20.66°	−179.21°	5.9	2.1
060716	2006/07/16	1424:04.7	600.7	−19.95°	−178.36°	5.7	1.7
060723	2006/07/23	2050:53.7	597.9	−17.97°	−178.42°	5.8	1.9
060802	2006/08/02	0047:06.3	454.2	−31.35°	179.70°	5.7	1.7
060815	2006/08/15	2353:51.2	162.5	−21.18°	−175.70°	6.1	2.8
060903	2006/09/03	2257:33.6	566.5	−23.97°	179.02°	5.9	2.2
070108	2007/01/08	2052:26.6	424.3	−18.50°	−177.66°	6.3	3.3
070409	2007/04/09	0224:32.5	613.7	−20.00°	−177.97°	5.9	2.3
070506	2007/05/06	2111:56.7	690.8	−19.44°	−179.04°	6.5	4.1
070925	2007/09/25	0516:05.0	419.4	−30.71°	−179.87°	6.2	3.0
071005	2007/10/05	0717:59.2	541.1	−25.30°	179.52°	6.5	4.3

[a]Date is given as year/month/day.

are at epicentral distances $\Delta > 80°$. At these distances, the difference between the arrival times of *S* and *ScS* waves is small. However, as waveform inversion can utilize data such as overlapped *S* and *ScS* phases, we can invert such data for the vertical profile of shear velocity in the lowermost mantle beneath the Pacific.

3.1. Waveform Data

[21] We use the transverse components of broadband waveform data (obtained by rotating the N-S and E-W components) for 26 events from the Incorporated Research Institutions for Seismology (IRIS) and Berkeley Digital Seismic Network (BDSN) data centers (Table 1 and Figure 3). Stations near the Pacific in North America including the USArray were chosen (Figure 3). We deconvolve the instrument response, and apply a band-pass filter to the data and construct data sets for the passband 0.005 to 0.125 Hz (i.e., for the period range, 8–200 s). We then select records which include data for *S*, *ScS*, and the other phases which arrive between them. We compute the ratio of the maximum amplitude of the data and the corresponding synthetic, and eliminate records for which the ratio is greater than 2 or less than 0.5. The data set consists of 1022 records that satisfy this criterion; 4801 records which did not satisfy the criterion were rejected. If there is too great a difference between the data and synthetics there is some danger the inversion will fall into a local minimum, so we excluded poorly fitting data. Actually, however, our experiments [*Konishi et al.*, 2009] suggest that we probably would not have obtained a significantly different model if the rejected data had been included in the data set. The data are velocity seismograms (with units of m s^{-1} after deconvolving the instrument response) with 1 Hz sampling. The reciprocal of the maximum amplitude of each record is used as the weighting factor in the inversion, so that all data have roughly the same importance.

3.2. Source Time Function and Static Correction

[22] The source parameters (moment tensors and centroids) are fixed to the global centroid moment tensor (CMT) solution. KTGF07 approximated the source time function as a δ function at the centroid time for the period range 20–200 s, since its effect is small. As this study, however, uses data for the period range 8–200 s, we use boxcar moment rate functions whose half duration is obtained from the global CMT solutions. We convolve the boxcar moment rate function with the synthetic seismograms and their partial derivatives in the frequency domain.

[23] The waveforms that sample the lowermost mantle pass through the crust, upper mantle, transition zone, and lower mantle, whose effects must be corrected for. We handle this by determining static corrections (time shifts) for the observed waveforms. KTGF07 made static corrections using the time shift that gives the best correlation coefficient between the synthetic and observed seismograms using the arrivals of direct *S* waves as the reference. However, as the *S* wave velocities within 500 km above the core-mantle boundary (CMB) are the unknown parameters in this study, we cannot use direct *S* waves as the reference at the epicentral distance range of our data set. Therefore, we infer δt_e and δt_s simultaneously with the other unknowns (i.e., the *S* wave velocities), where δt_e and δt_s are the time shifts for the events and stations, respectively. We use the temporal derivatives of the synthetics as the partial derivatives with respect to the time shift. To avoid instabil-

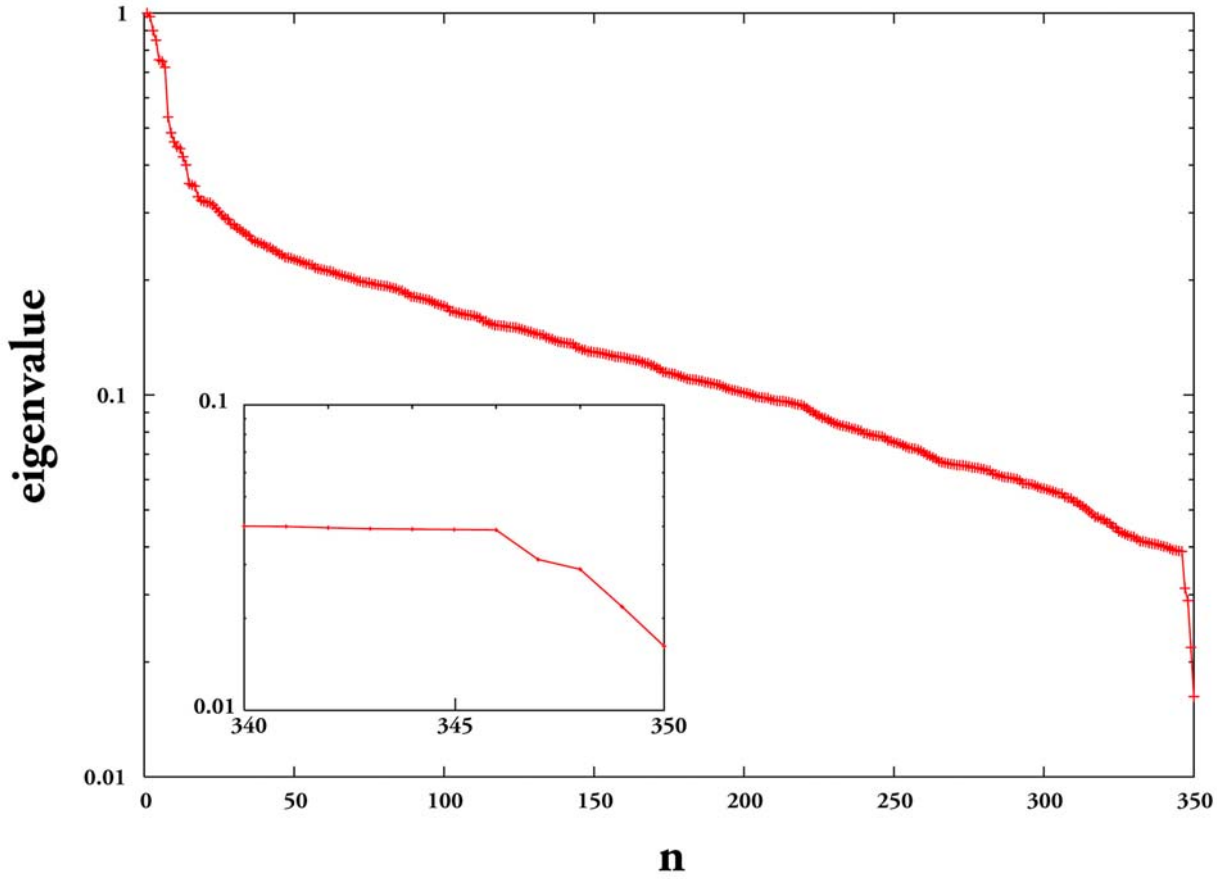

Figure 4. Absolute values of SVD eigenvalues for the inversion in Figure 5, with the largest normalized to one. The first 26 modes primarily give information on source corrections, the next 319 modes give information on station corrections, and the final 50 modes give information on Earth structure. Because the magnitude of the eigenvalues falls rapidly after $n = 346$, only the first 350 eigenvalues are shown. The 340th through 350th eigenvalues are shown in the inset.

ity, we reject events with records from less than three stations.

3.3. Inversion

[24] The initial model is anisotropic preliminary reference Earth model (PREM) [*Dziewonski and Anderson*, 1981]. The source parameters (moment tensors, centroids, and half durations) are fixed to the global CMT solution. In this study the *S* wave velocities at points 500 km above the CMB and higher are fixed to PREM, while those within 500 km of the CMB are the unknown parameters.

[25] Since the existence of low *S* velocities in the target region is well known [e.g., *Grand*, 2002], it is inappropriate to use PREM as the starting model for the final inversion. We therefore began by conducting inversion for a vertically averaged model that is appropriate to be used as the starting model for the final inversion. We conducted an inversion without making any static corrections, and used only the eigenvector corresponding to the largest eigenvalue of the singular value decomposition (SVD) [e.g., *Wiggins*, 1972] of the matrix of partial derivatives as the basis function for the perturbation to the starting model and obtained a model with basically a constant velocity (about 7.14 km s^{-1}) in the depth range from 2471 to 2891 km (i.e., for the lowermost 420 km of the mantle). We use a smoothed version of this model, which we call PREM′, as the starting model in our inversions.

[26] The initial model for the final inversion is the PREM′ model (in the deepest mantle) in combination with anisotropic PREM (at shallower depths). The number of unknown parameters is 395 (50 *S* wave velocities in each 10 km depth interval, 26 time shifts for the events and 319 for the stations). We conduct inversions using the eigenvectors corresponding to the *n* largest eigenvalues of SVD of the matrix of partial derivatives as the basis functions of the perturbation to the starting model.

[27] The absolute values of the SVD eigenvalues (largest normalized to one) are shown in Figure 4. In general, each SVD eigenvector contains components related to all of the variables (source and station corrections and Earth structure). However, it appears (Figure 4) that the first 26 eigenvectors are primarily dominated by source corrections, the next 319 by station corrections, and the final 50 (346–395) by Earth structure. We therefore conduct inversions using at least 346 eigenvectors.

[28] The results of our inversions for $n = 346, \ldots, 350$ are shown in Figure 5. All five of the models in Figure 5 are basically similar. They all show a decrease in *S* velocity of about 0.15 km s^{-1} in the depth range from 2400 to 2600 km, and an increase of about 0.2 km s^{-1} from 2600 to 2800 km,

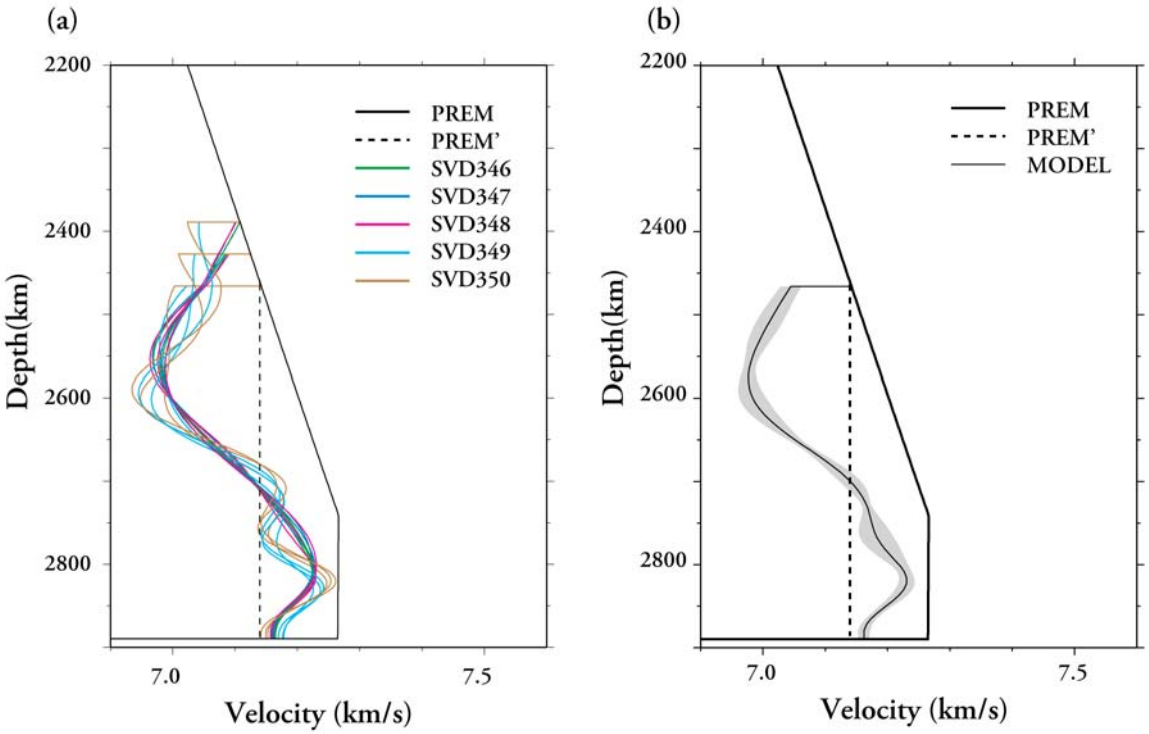

Figure 5. Results of the inversion. (a) We show 15 models for each SVD parameterization (SVD346–350) for each tie-in depth (420, 460, and 500 km). All of the velocity models show the same general features. (b) The averaged model shows the same "S"-shaped model as shown by *Konishi et al.* [2009]. The error bar is one standard deviation using 15 models as independent.

and a decrease of about 0.1 km s^{-1} from 2800 km to the CMB.

[29] Table 2 shows the variance and the Akaike information criterion (AIC) [*Akaike*, 1977] values for PREM and PREM′ and for the five corresponding SVD inversions. AIC is a statistical measure that rewards variance reduction and penalizes increases in the number of model parameters. Lower values of AIC denote models which are formally better, in a statistical sense. We assume the effective number of independent data is 12.5% (1/8) of the above numbers of data points because the data are sampled at 1 Hz but are low-passed filtered to exclude periods shorter than 8 s. Note that the number of free parameters is 0 for PREM, 1 for PREM′, 346 for SVD346, and so on. Despite the large increase in k, all of the inversions yield a lower value of AIC than that for PREM or PREM′, which confirms the statistical significance of the variance reduction achieved by the SVD inversions. The best (lowest) variance and AIC values are obtained for SVD346. Note that the variance values used in Table 2 are not from the linearized inversion, but rather from an exact forward calculation for each model. *Konishi et al.* [2009] present a detailed discussion of AIC, which is a statistical measure that rewards variance reduction and penalizes extra unknown model parameters. Lower AIC values suggest model preferability.

[30] The fact that variance for all of the models in Table 2 is in excess of 100% might raise some questions about the meaningfulness of the inversion. If there were only a small number of data, such questions might well be reasonable. However, as noted above, we started with 5823 records, picked the best 1022 of these, and then simultaneously inverted this entire data set. The various statistical and visual tests presented in this section confirm the robustness of the inversion results, this variance notwithstanding. Also note that the variance values in Table 2 were calculated exactly with respect to each model rather than estimated using the Born approximation. The increase for the final few entries is due to the nonlinearity of the inversion.

3.4. Robustness

[31] We vary two parameters to examine the robustness of the inversion results. The first, which we call the "tie-in depth," is the depth above which the model is fixed to the initial model (PREM/PREM′), with an S velocity discontinuity allowed at the tie-in depth; we invert for tie-in depths of 420, 460, and 500 km above the CMB, respectively (i.e., for the coefficients of the 387, 391, and 395 eigenvectors used in the respective inversions). The second parameter, which

Table 2. Variance and AIC for Each Model Whose Tie-in Depth Is 500 km[a]

Model	Variance (%)	AIC
PREM	157.9	34618
PREM′	141.7	33483
SVD346	116.1	32079
SVD347	116.2	32090
SVD348	116.7	32137
SVD349	119.6	32397
SVD350	118.8	32329

[a]The time shifts for each station and each event ("static correction") are also determined as the unknowns.

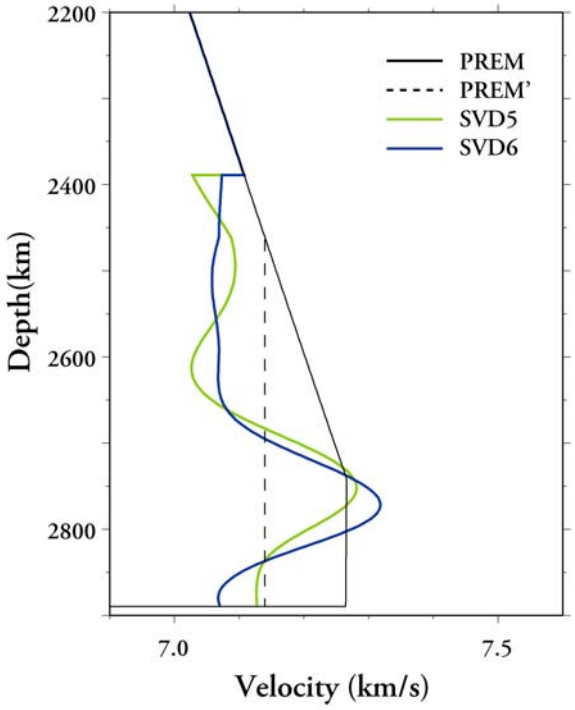

Figure 6. The results of inversions without static corrections. We obtained two similar *S* wave velocity models (SVD5, SVD6). The pattern of velocity structure is similar to Figure 5, but the absolute velocities differ slightly.

is varied, is the number of eigenvectors of the SVD used as the basis in each inversion; we invert for models using the eigenvectors corresponding to the first 346 to 350 eigenvalues of the SVD decomposition as the basis; these models are labeled SVD346 to SVD350. As discussed above, in actual practice the first 345 eigenvectors are dominated by the source and station corrections, while the 346th and subsequent eigenvectors reflect Earth structure in the target region.

[32] The 5 × 3 = 15 models obtained by the inversions varying the above parameters are shown in Figure 5. PREM and PREM′ are also shown for reference. Figure 5 shows that all of the models have basically the same general depth dependence. There is a velocity decrease in the depth range 2600–2700 km and a relative velocity increase in the depth range 2700–2800 km. The velocity then decreases somewhat as the CMB is approached.

3.4.1. Static Corrections

[33] We examine the question of whether the time shifts ("static corrections") could be causing artifacts in the velocity model. To address this question, we conducted several inversions relative to PREM′ without any time shifts. The resulting models for SVD5 and SVD6 are shown in Figure 6. The models obtained have essentially the same character as the models obtained by the actual inversions (Figure 5), except that the absolute velocities are shifted. Thus, we conclude that the pattern of depth dependence of the velocity models is not an artifact of the static corrections.

3.4.2. Synthetic Resolution Tests

[34] We conduct synthetic resolution ("checkerboard") tests to examine the ability of our methods to resolve various synthetic structure models. Since the input models are synthetic, there are no static corrections. We conducted tests for three model perturbations (Figure 7). Synthetic seismograms were calculated exactly for these two models and then used as the input for inversions relative to PREM′. As shown in Figure 7, the three-layered and four-layered input models could be recovered satisfactorily, although not perfectly.

3.4.3. Stacked Waveforms

[35] Some researchers may harbor doubts because waveform inversion is a "black box" procedure. Ideally, it would

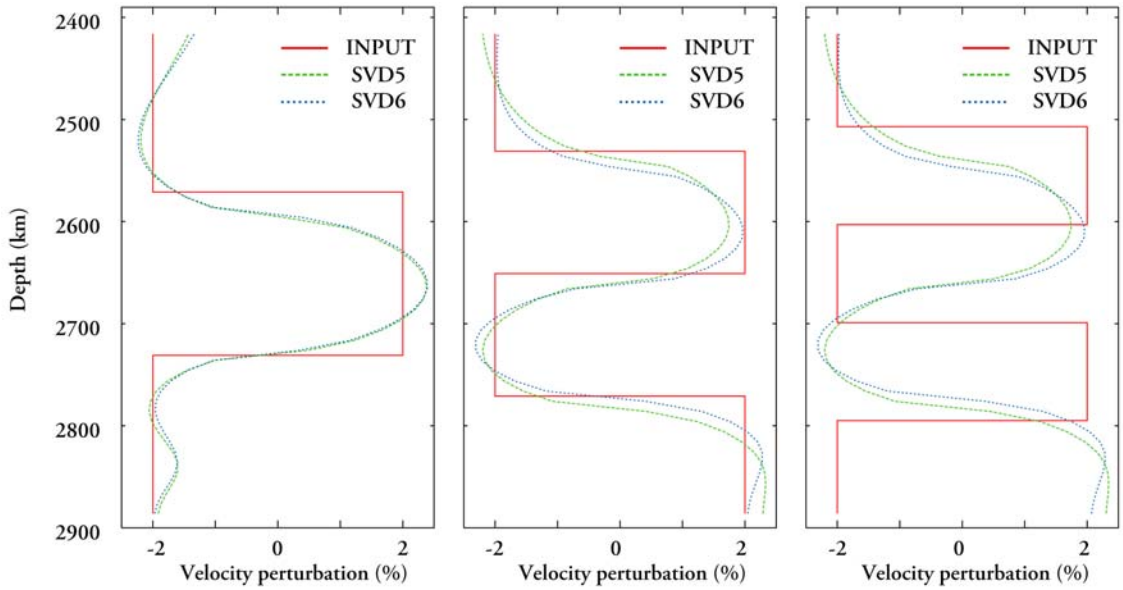

Figure 7. Synthetic resolution test ("checkerboard test") for D″ structure. Our methods and present data set can successfully resolve the three- and four-layered models, but the five-layered model cannot be resolved.

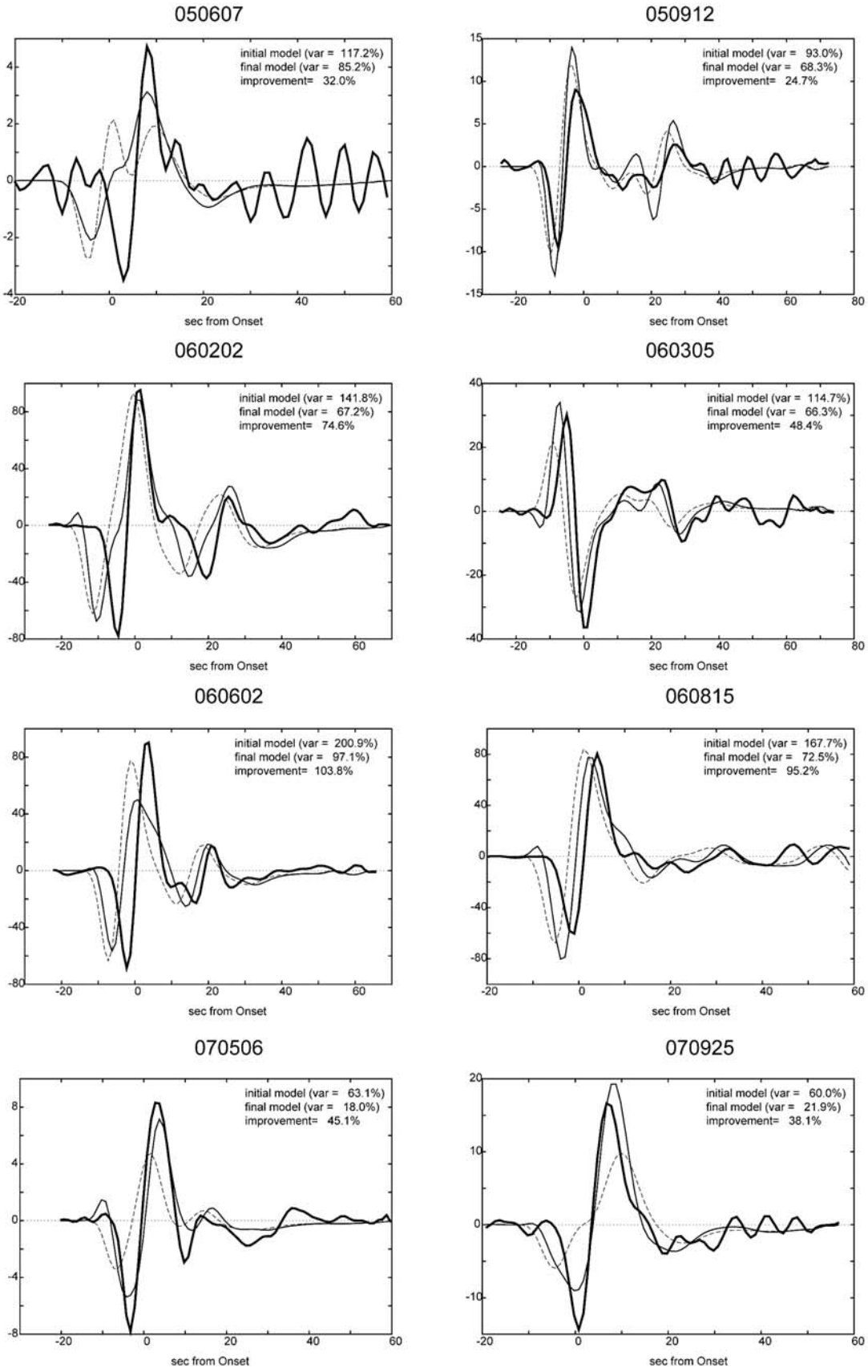
050607
initial model (var = 117.2%)
final model (var = 85.2%)
improvement= 32.0%
sec from Onset
050912
initial model (var = 93.0%)
final model (var = 68.3%)
improvement= 24.7%
sec from Onset
060202
initial model (var = 141.8%)
final model (var = 67.2%)
improvement= 74.6%
sec from Onset
060305
initial model (var = 114.7%)
final model (var = 66.3%)
improvement= 48.4%
sec from Onset
060602
initial model (var = 200.9%)
final model (var = 97.1%)
improvement= 103.8%
sec from Onset
060815
initial model (var = 167.7%)
final model (var = 72.5%)
improvement= 95.2%
sec from Onset
070506
initial model (var = 63.1%)
final model (var = 18.0%)
improvement= 45.1%
sec from Onset
070925
initial model (var = 60.0%)
final model (var = 21.9%)
improvement= 38.1%
sec from Onset

Figure 8

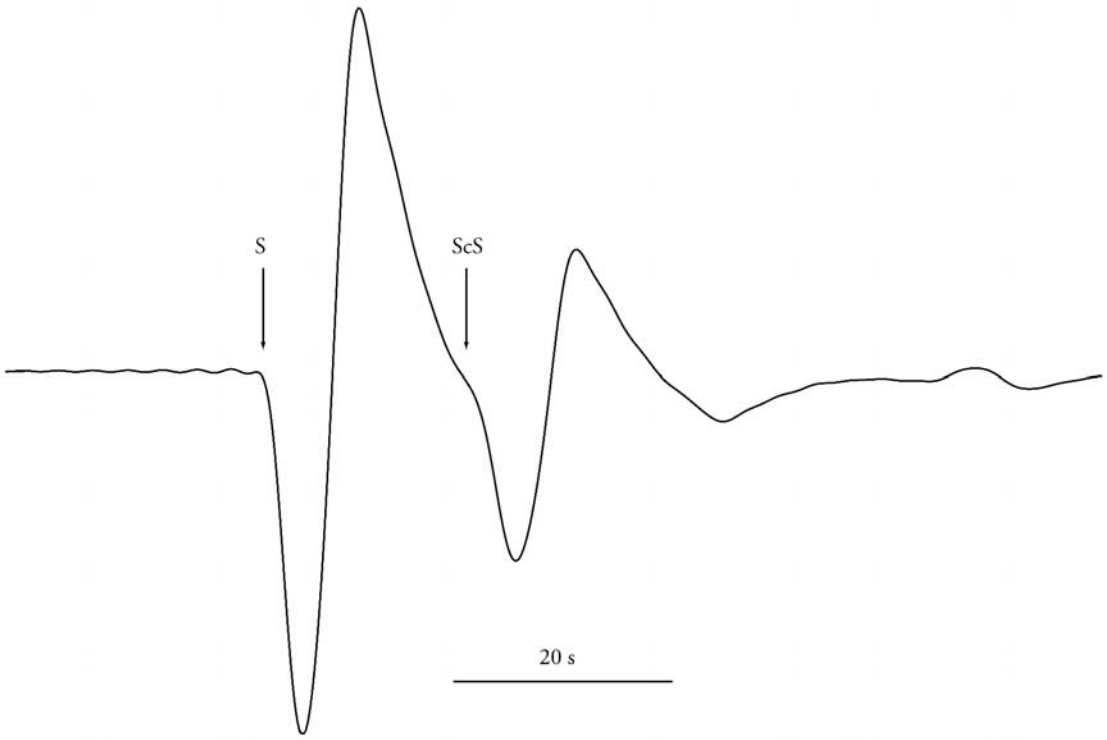

Figure 9. The transverse component of synthetics low-pass filtered below 3 s period for an event on 060602 at station CMB for the PREM model. A box-car source time function is convolved with the synthetics. The arrows indicate the theoretical arrival time of *S* and *ScS* phases.

be possible to look at the observed waveforms for individual stations and to compare them to synthetics for PREM and for the final model to see visually as well as quantitatively the improvement in the fit. Unfortunately, however, the noise level is too high to allow meaningful visual study of data and synthetics for individual records. We therefore have prepared ''quality control stacks'' (QC stacks), some of which are shown in Figure 8, for some of the events in this study. These stacks are not intended for use in obtaining the Earth model but rather merely as a check to ensure that the inversion result is reasonable. The stacks are made by aligning the records (after station and source corrections) using the PREM arrival time and normalizing the maximum amplitude of each of the observed records to one. The synthetics are processed using the same weighting factors as the corresponding observed record. Model SVD346 (with a tie-in depth of 500 km) was used as the final model. We show QC stacks for 8 of the 27 events. The QC stacks shown in Figure 8 are typical examples, and those for the other events are basically similar. The QC stacks in Figure 8 show that the synthetics for the final model are, overall, a clear improvement over those for the initial model, thereby confirming that the inversion has reached a reasonable result.

4. Discussion: Resolvability of 3-D Structure

[36] There have been several previous studies on D″ beneath the Pacific using Tonga-Fiji events. As almost stations in North America are at epicentral distances of 85° or greater and *S* and *ScS* phases are overlapped at these epicentral distances, it is difficult for methods other than waveform inversion to utilize such data. Previous studies therefore have been limited in terms of available data and regions studied. For example, *Ritsema et al.* [1997] studied the vertical dependence of shear wave velocity in the lower mantle beneath the Pacific using *S*diff-*SKS* travel time residuals and found a strong negative gradient. However, the resolution of diffracted shear waves is basically limited to resolving only the average shear velocity in D″, even if a large data set is used [*Kawai et al.*, 2007b]. Also, *SKS* phases are affected by core structure.

[37] Recently, methods from exploration geophysics such as double-array stacking [e.g., *Avants et al.*, 2006a] have also been used to study D″. As such studies use data from a

Figure 8. ''Quality control stacks'' for eight events, computed as follows. First, all of the observed waveforms for each event were time shifted using PREM, after making the same source and station corrections as in the inversion. These waveforms were then filtered in the passband for 8 s to 200 s using a four-pole band-pass filter. The maximum amplitude of each observed record was normalized to one, and the waveforms were then stacked (thick curves). The synthetics for the initial model (PREM, dotted curves) and final model (thin solid curves) were stacked using the same weighting factors as for the corresponding observed record. Model SVD346 (with a tie-in depth of 500 km) was used as the final model.

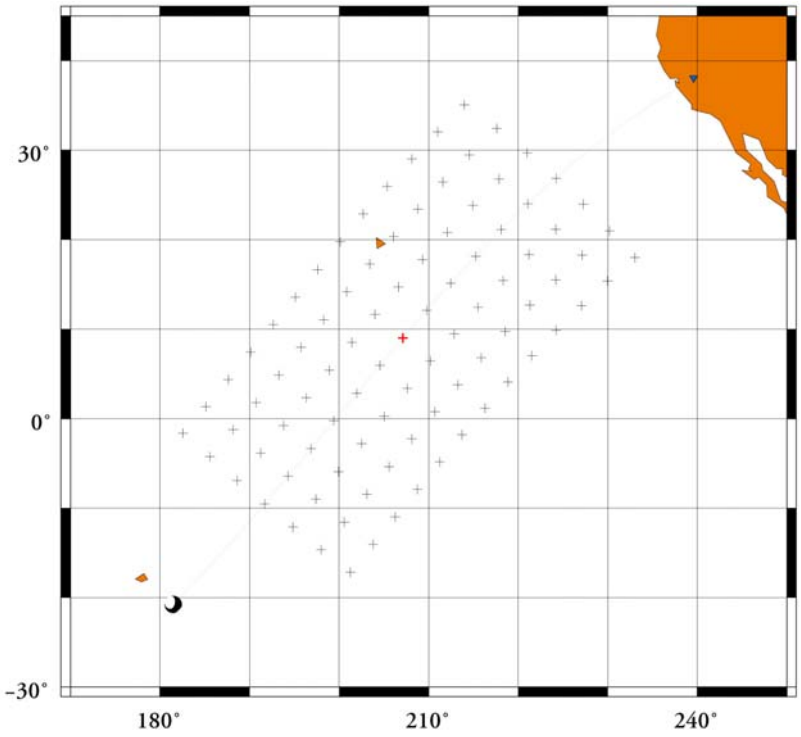

Figure 10. The geometry of the sensitivity analysis. A south of Fiji Islands event on 060602 (with a centroid depth 584.6 km and a moment magnitude of M_w = 6.0) and station CMB (longitude of 38.0°, longitude of 239.7°) are used. The epicentral distance is 80.0°. The raypath between the source and station is shown. The blue inverted triangle, red plus, and black pluses show the location of the station, bottoming point at the CMB of the *ScS* phase, and the voxels, respectively.

narrow range of epicentral distances (e.g., from 74° to 83° [see *Avants et al.*, 2006a]), the data sample only a small range of incidence angles. *Avants et al.* [2006b] and *Lay et al.* [2006] proposed a detailed laterally heterogeneous model for D″ beneath the western Pacific based on double-array stacking analysis. They used the transverse component of seismograms at frequencies up to 0.3 Hz for Tonga-Fiji events and stations in western northern America at epicentral distances from 74° to 85°. They binned data according to the bounce point of *ScS* phases at the CMB, stacked waveforms, obtained reflection amplitudes, and interpreted them to obtain a model of the vertical dependence of shear wave velocity. They combined the binned models to construct a laterally heterogeneous model of the lowermost mantle beneath the Pacific at intervals of about 4°. Such studies do not use a quantitative inversion procedure and cannot easily quantify the resolving power of their data. We consider these points below.

[38] Rather than attempting to duplicate the methodology of the above studies, we calculate synthetic seismograms of the same type as those in the above studies and then analyze the inherent resolving power of such data. We proceed as follows. We first calculate synthetic seismograms and partial derivatives for a laterally homogeneous model (PREM) down to a minimum period of 3 s (i.e., for a maximum frequency of 0.333 Hz). We then conduct numerical experiments to test the extent to which this data set can resolve laterally heterogeneous structure. We estimate the sensitivity to structure in the lowermost mantle of *S* and *ScS* waveforms observed at station, CMB (latitude of 38.0°N, longitude of 59.7°W), for the 060602 event (see Table 1) beneath Fiji (epicentral distance of 80.0°) at periods up to 3 s using the formulation in section 2.1.1. The synthetic is shown in Figure 9.

[39] We compute partial derivatives with respect to finite voxels (4° × 4° × 10 km) in volumes along the great circle of the bounce point within ±24° in the plane of the great circle and within ±12° in the direction perpendicular to the great circle for depths up to 500 km above the CMB (Figure 10). We compute "sensitivities" for perturbations to each voxel. We define "sensitivity" as follows:

$$S_i^{(kpl)} = \int_{t_0}^{t_1} \left(\frac{\partial u_i^{(k)}\left[\mathbf{r}^{(p)}\right]}{\partial m_l} \right)^2 dt, \tag{13}$$

where $S_i^{(kpl)}$ is the sensitivity of the *i*th component of the displacement at the *p*th receiver for the *k*th earthquake with respect to a perturbation to the *l*th model parameter.

[40] We first investigate the sensitivity of a time window that includes both *S* and *ScS* phases for four different period ranges for partials along the great circle (Figure 11). We find that the sensitivity is greatest at the *ScS* bounce point for all period ranges. Also, we see in Figure 11 that the *S* and *ScS* phases have sensitivity along their entire propagation paths, especially within ±6° of the *ScS* bounce point immediately above the CMB. Note that the smearing becomes more extensive as the cutoff period of the filter increases (Figures 11b–11d). We also estimate sensitivities for the windows containing mainly the *S* phase (Figure 11e, based on *S* and

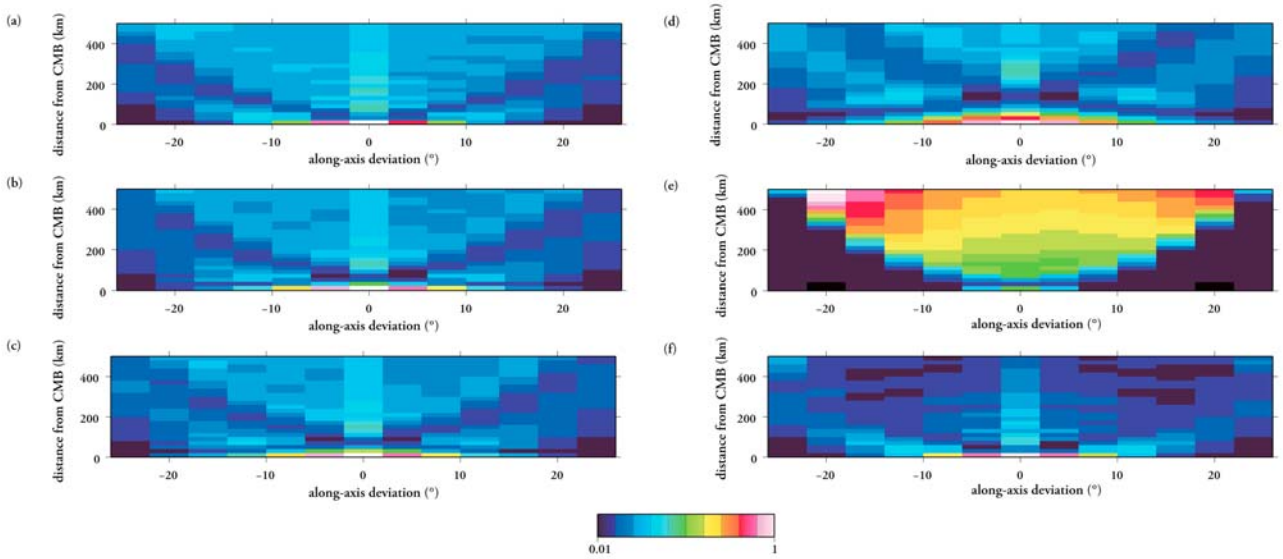

Figure 11. The sensitivities (see equation (13)) for a time window that includes both *S* and *ScS* phases for points along the great circle path for data low-pass filtered below periods of (a) 3 s, (b) 8 s, (c) 10 s, and (d) 20 s, respectively. The horizontal axis indicates the along-axis deviation from the bounce point of the *ScS* phase (see Figure 10). The sensitivities are normalized to a maximum of one. (e and f) The sensitivities for a low-pass filter below a period of 3 s along the great circle path for the *S* and *ScS* windows.

ScS arrival times computed for PREM) and for the *ScS* window (35 s from the *ScS* arrival, also based on PREM, Figure 11f). For *ScS* only (Figure 11f), sensitivities are smeared out over a wider range than those for the combined *S*-*ScS* window (Figure 11a). This confirms the efficacy of using the combined *S*-*ScS* data set to investigate structure in the lowermost mantle.

[41] Next, we estimate sensitivities off the great circle axis around the *ScS* bounce point (Figure 12). The most sensitive region (white) is actually off the great circle due to the source mechanism (Figure 10). This example demonstrates the limitations of the great circle approximation and suggests that later phases such as *ScS* can be affected by scattering due to lateral heterogeneity.

[42] In addition, we compute the correlation coefficient of partials away from the bounce point (Figure 13). Using waveforms low-pass filtered even at periods above 3 s, correlation coefficients at a distance of 4° along the great circle are over 0.7 (Figure 13a). This suggests that binning along the axis in a narrow range of epicentral distances may not accurately resolve lateral heterogeneity. Coefficients off the great circle show negative large correlations over 0.6 (Figure 13b). This is due to side lobe effects. Next the depth dependence of the correlation coefficients is shown (Figure 13c). This may indicate that the vertical resolution of waveforms at frequencies up to 0.33 Hz is at best 40 km.

[43] The results in Figures 11–13 suggest, but do not prove, that studies which use geometrical optics to infer the 3-D structure of the lowermost mantle might be overestimating their ability to resolve lateral and vertical heterogeneity. On the other hand, although, as discussed in section 2, our methods are formulated to allow waveform inversion for 3-D structure, we have not yet carried out such studies. Since waveform inversion allows full use of all information in all of the recorded seismograms (especially overlapped phases), it seems reasonable to state that waveform inversion for the 3-D structure can place an upper limit on our ability to resolve the 3-D structure of the mantle using data of a given type and a given frequency range. We plan to carry out such studies in the near future.

5. Geophysical Implications

[44] It has been suggested that D″ in the large-scale low shear velocity region beneath the Pacific is chemically distinct from D″ in other regions because of dense debris of subducted oceanic slabs [e.g., *Tackley*, 2000], which accumulated when the Rodinia supercontinent was created [*Maruyama et al.*, 2007]. The remnants of dense MORB crust, which includes Al- and Fe-rich Mg-perovskite and $CaCl_2$-type SiO_2, are thus expected to have accumulated in D″ beneath the Pacific [e.g., *Christensen and Hofmann*, 1994].

[45] In this paper, we studied the fine structure of D″ in the eastern part of the large low shear velocity region. We found 1%–1.5% velocity decreases and increases in the zones from 400 to 500 km and from 300 to 400 km above the CMB, respectively. In addition, we found 0.5%–1% velocity increases and decreases in the zones from 100 to 200 km and from 0 to 100 km above the CMB, respectively. These velocity structures are interpreted in terms of a phase transition model based on experimental results for phase transitions in pyrolite [*Ohta et al.*, 2008] (although a chemical stratification model, e.g., *Maruyama et al.* [2007], cannot be excluded). The upper velocity decrease is interpreted as due to the phase transitions in basalt from Mg-pv to Mg-ppv [*Tsuchiya and Tsuchiya*, 2006] and from $CaCl_2$-type to α-PbO_2-type SiO_2 [*Karki et al.*, 1997], and the upper velocity increase is interpreted as due to the phase transition in pyrolite from pv to ppv [*Tsuchiya et al.*, 2004].

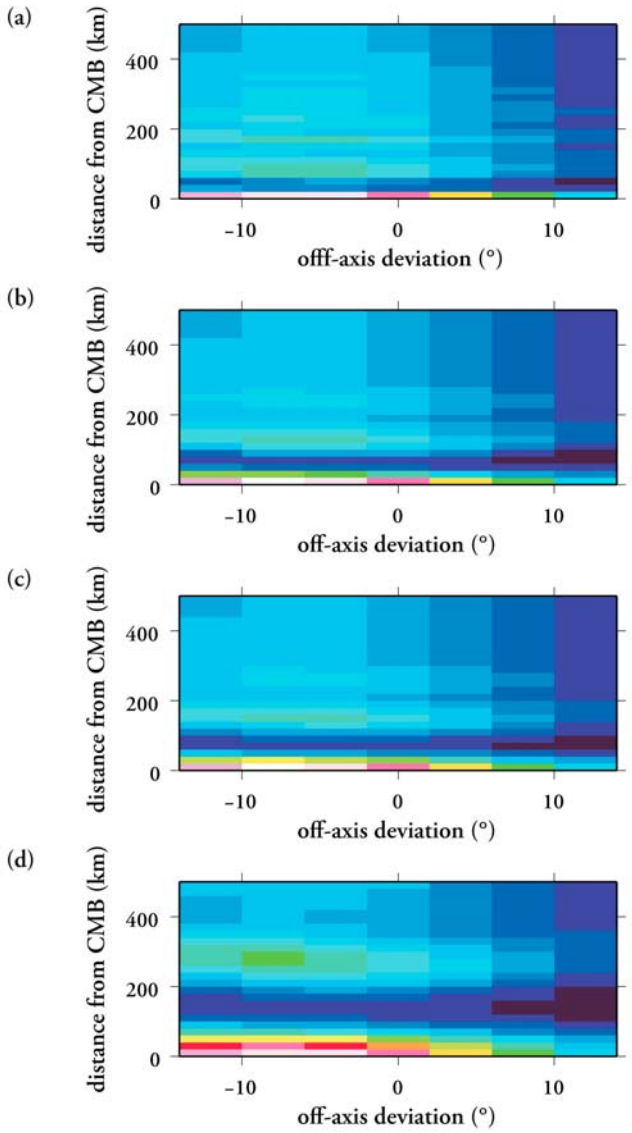

Figure 12. The sensitivities for a time window that includes both *S* and *ScS* phases are shown for low-pass filters with cutoff periods of (a) 3 s, (b) 8 s, (c) 10 s, and (d) 20 s. The horizontal axis indicates the off-axis deviation from the bounce point of the *ScS* phase. The sensitivities are normalized to a maximum sensitivity of one. The bias of amplitudes in the respective directions away from the bounce point is due to the source mechanism.

Also, the lower velocity decrease could be interpreted as due to the reverse phase transitions from ppv to pv, called a ''double crossing'' [*Hernlund et al.*, 2005], or due to temperature increase [*Kawai and Tsuchiya*, 2009]. The velocity decrease and increase occur in a depth range of about 100 km, which is a 6 GPa pressure range. This is consistent with experimental results for phase relations in pyrolite and basalt [*Ohta et al.*, 2008]. Therefore, the obtained model suggests that a mixture of MORB and pyrolitic materials exist in this region. The occurrence of the inferred phase transitions from pv to ppv over a depth range of 100 km may be due to solution of Al and Fe [*Tsuchiya and Tsuchiya*, 2008].

[46] Our previous study of D″ beneath Central America [*Kawai et al.*, 2007a] found an *S* wave velocity of about 7.25 km s^{-1} immediately above the CMB, which is about 0.09 km s^{-1} faster than the velocity obtained in this study

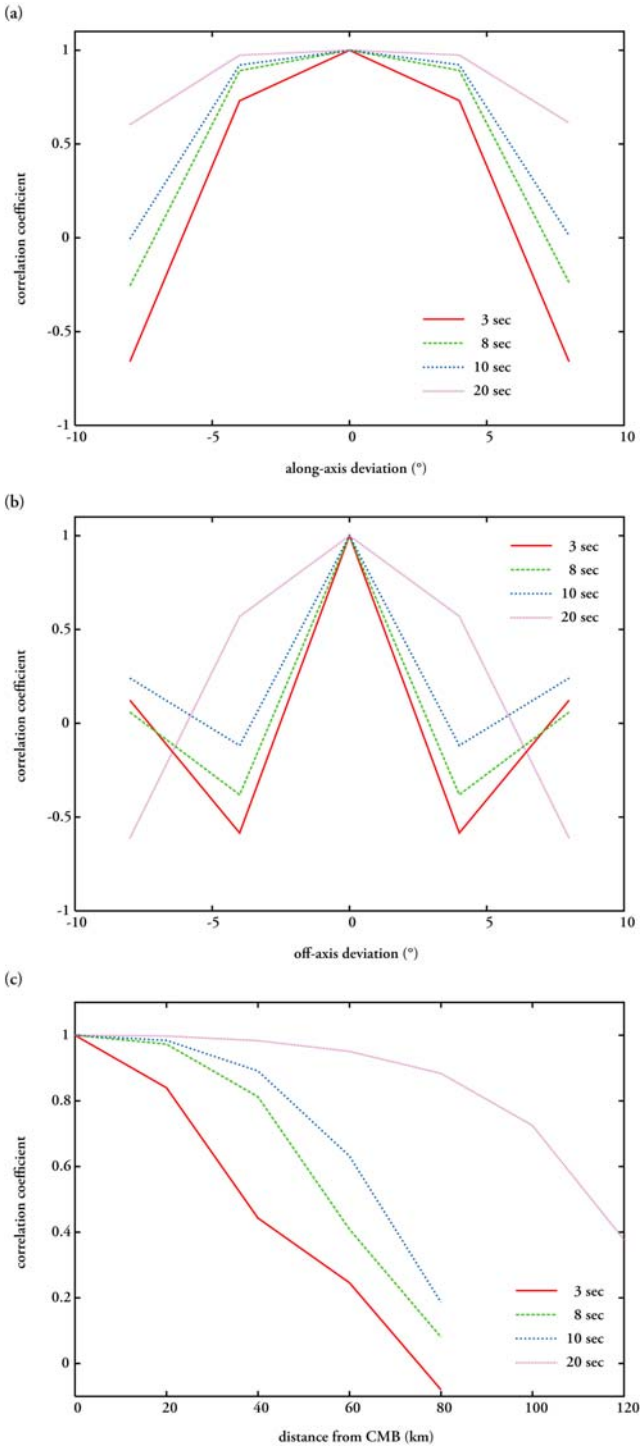

Figure 13. The correlations of partial derivatives with respect to perturbations between the partials at the bounce point of the *ScS* phase and at the other point are shown for periods of 3, 8, 10, and 20 s, respectively. The correlations for (a) along-axis, (b) off-axis, and (c) depth dependence (distance from CMB) are shown.

(about 7.16 km s^{-1}). The mantle is thought to contain impurities such as aluminum and iron [*Ringwood*, 1962]. With the assumption of isothermal conditions immediately above the CMB, the above velocity difference can be attributed to difference in chemical composition. *Tsuchiya and Tsuchiya* [2006] showed that impurities in Mg-pv decrease the shear wave velocity. For example, a 1 mol % increase in the amount of both aluminum and iron causes a 0.303% S velocity decrease in Mg-pv or a 0.367% S velocity decrease in Mg-ppv. Hence, the amount of impurities in Mg-pp/ppv beneath the Pacific is 3.5–4 mol % larger than that beneath Central America, on the assumption that the ratio of aluminum and iron is the same for both regions. As the PREM model can be approximated as pyrolite composition with 7 mol % impurities [e.g., *McDonough and Sun*, 1995], we estimate the amount of impurities in Mg-pv beneath the Pacific to be 10 mol%. Combined with the result of *Konishi et al.* [2009], who found a shear velocity of 7.18 km s^{-1} immediately above the CMB in the western Pacific, the large low shear velocity province (LLSVP) beneath the Pacific includes a larger amount of impurities than the mantle average, but it may contain a smaller amount of impurities than would be expected for a basaltic composition (>20 mol %) [*Ohta et al.*, 2008; *Konishi et al.*, 2009].

Appendix A: Explicit Expressions for Partial Derivatives

[47] We use a δ function as the spatial dependence of the model parameters in computation of partial derivatives for a voxel perturbation, i.e., $\rho^{(l)} = \delta\rho\delta(\mathbf{r} - \mathbf{r_0})$ or $C^{(l)}_{ijpq} = \delta C_{ijpq}\,\delta(\mathbf{r} - \mathbf{r_0})$. As the perturbation to the elastic parameters is expressed as $C^{(l)}_{ijpq}$, we can easily formulate the partial derivatives for general anisotropy and for the anelastic parameter Q.

A1. Transversely Isotropic Case

[48] Here, we present explicit expressions for the kernels of the partial derivatives with respect to the elastic constants for the transversely isotropic case:

$$
\begin{aligned}
&-\left[u^{(k)}_{j,q}\right]^{*}\left[C^{(l)}_{jqrs}\right]^{*}\eta^{(p)}_{ri,s}\\
=\;&-\left[u^{(k)}_{x,x}\right]^{*}\left[C^{(l)}_{xxxx}\right]^{*}\eta^{(p)}_{xi,x}-\left[u^{(k)}_{y,y}\right]^{*}\left[C^{(l)}_{yyyy}\right]^{*}\eta^{(p)}_{yi,y}-\left[u^{(k)}_{z,z}\right]^{*}\left[C^{(l)}_{zzzz}\right]^{*}\eta^{(p)}_{zi,z}\\
&-\left[u^{(k)}_{x,x}\right]^{*}\left[C^{(l)}_{xxyy}\right]^{*}\eta^{(p)}_{yi,y}-\left[u^{(k)}_{y,y}\right]^{*}\left[C^{(l)}_{yyzz}\right]^{*}\eta^{(p)}_{zi,z}-\left[u^{(k)}_{z,z}\right]^{*}\left[C^{(l)}_{zzxx}\right]^{*}\eta^{(p)}_{xi,x}\\
&-\left[u^{(k)}_{x,x}\right]^{*}\left[C^{(l)}_{xxzz}\right]^{*}\eta^{(p)}_{zi,z}-\left[u^{(k)}_{z,z}\right]^{*}\left[C^{(l)}_{zzyy}\right]^{*}\eta^{(p)}_{yi,y}-\left[u^{(k)}_{y,y}\right]^{*}\left[C^{(l)}_{yyxx}\right]^{*}\eta^{(p)}_{xi,x}\\
&-\left[u^{(k)}_{x,y}\right]^{*}\left[C^{(l)}_{xyxy}\right]^{*}\eta^{(p)}_{xi,y}-\left[u^{(k)}_{x,y}\right]^{*}\left[C^{(l)}_{xyyx}\right]^{*}\eta^{(p)}_{yi,x}-\left[u^{(k)}_{y,x}\right]^{*}\left[C^{(l)}_{yxxy}\right]^{*}\eta^{(p)}_{xi,y}-\left[u^{(k)}_{y,x}\right]^{*}\left[C^{(l)}_{yxyx}\right]^{*}\eta^{(p)}_{yi,x}\\
&-\left[u^{(k)}_{y,z}\right]^{*}\left[C^{(l)}_{yzyz}\right]^{*}\eta^{(p)}_{yi,z}-\left[u^{(k)}_{y,z}\right]^{*}\left[C^{(l)}_{yzzy}\right]^{*}\eta^{(p)}_{zi,y}-\left[u^{(k)}_{z,y}\right]^{*}\left[C^{(l)}_{zyyz}\right]^{*}\eta^{(p)}_{yi,z}-\left[u^{(k)}_{z,y}\right]^{*}\left[C^{(l)}_{zyzy}\right]^{*}\eta^{(p)}_{zi,y}\\
&-\left[u^{(k)}_{z,x}\right]^{*}\left[C^{(l)}_{zxzx}\right]^{*}\eta^{(p)}_{zi,x}-\left[u^{(k)}_{z,x}\right]^{*}\left[C^{(l)}_{zxxz}\right]^{*}\eta^{(p)}_{xi,z}-\left[u^{(k)}_{x,z}\right]^{*}\left[C^{(l)}_{xzzx}\right]^{*}\eta^{(p)}_{zi,x}-\left[u^{(k)}_{x,z}\right]^{*}\left[C^{(l)}_{xzxz}\right]^{*}\eta^{(p)}_{xi,z}
\end{aligned}
\tag{A1}
$$

$$
\begin{aligned}
=\;&-\left[u^{(k)}_{x,x}\right]^{*}\left[A^{(l)}\right]^{*}\eta^{(p)}_{xi,x}-\left[u^{(k)}_{y,y}\right]^{*}\left[A^{(l)}\right]^{*}\eta^{(p)}_{yi,y}-\left[u^{(k)}_{z,z}\right]^{*}\left[C^{(l)}\right]^{*}\eta^{(p)}_{zi,z}\\
&-\left[u^{(k)}_{x,x}\right]^{*}\left[H^{(l)}\right]^{*}\eta^{(p)}_{yi,y}-\left[u^{(k)}_{y,y}\right]^{*}\left[F^{(l)}\right]^{*}\eta^{(p)}_{zi,z}-\left[u^{(k)}_{z,z}\right]^{*}\left[F^{(l)}\right]^{*}\eta^{(p)}_{xi,x}\\
&-\left[u^{(k)}_{x,x}\right]^{*}\left[F^{(l)}\right]^{*}\eta^{(p)}_{zi,z}-\left[u^{(k)}_{z,z}\right]^{*}\left[F^{(l)}\right]^{*}\eta^{(p)}_{yi,y}-\left[u^{(k)}_{y,y}\right]^{*}\left[H^{(l)}\right]^{*}\eta^{(p)}_{xi,x}\\
&-\left[u^{(k)}_{x,y}\right]^{*}\left[N^{(l)}\right]^{*}\eta^{(p)}_{xi,y}-\left[u^{(k)}_{x,y}\right]^{*}\left[N^{(l)}\right]^{*}\eta^{(p)}_{yi,x}-\left[u^{(k)}_{y,x}\right]^{*}\left[N^{(l)}\right]^{*}\eta^{(p)}_{xi,y}-\left[u^{(k)}_{y,x}\right]^{*}\left[N^{(l)}\right]^{*}\eta^{(p)}_{yi,x}\\
&-\left[u^{(k)}_{y,z}\right]^{*}\left[L^{(l)}\right]^{*}\eta^{(p)}_{yi,z}-\left[u^{(k)}_{y,z}\right]^{*}\left[L^{(l)}\right]^{*}\eta^{(p)}_{zi,y}-\left[u^{(k)}_{z,y}\right]^{*}\left[L^{(l)}\right]^{*}\eta^{(p)}_{yi,z}-\left[u^{(k)}_{z,y}\right]^{*}\left[L^{(l)}\right]^{*}\eta^{(p)}_{zi,y}\\
&-\left[u^{(k)}_{z,x}\right]^{*}\left[L^{(l)}\right]^{*}\eta^{(p)}_{zi,x}-\left[u^{(k)}_{z,x}\right]^{*}\left[L^{(l)}\right]^{*}\eta^{(p)}_{xi,z}-\left[u^{(k)}_{x,z}\right]^{*}\left[L^{(l)}\right]^{*}\eta^{(p)}_{zi,x}-\left[u^{(k)}_{x,z}\right]^{*}\left[L^{(l)}\right]^{*}\eta^{(p)}_{xi,z},
\end{aligned}
$$

where $H = A - 2N$. Also, we can write this in spherical coordinates as

$$
\begin{aligned}
&-\left[u^{(k)}_{j,q}\right]^{*}\left[C^{(l)}_{jqrs}\right]^{*}\eta^{(p)}_{ri,s}\\
=\;&-\left[u^{(k)}_{\theta,\theta}\right]^{*}\left[A^{(l)}\right]^{*}\eta^{(p)}_{\theta i,\theta}-\left[u^{(k)}_{\phi,\phi}\right]^{*}\left[A^{(l)}\right]^{*}\eta^{(p)}_{\phi i,\phi}-\left[u^{(k)}_{r,r}\right]^{*}\left[C^{(l)}\right]^{*}\eta^{(p)}_{ri,r}\\
&-\left[u^{(k)}_{\theta,\theta}\right]^{*}\left[H^{(l)}\right]^{*}\eta^{(p)}_{\phi i,\phi}-\left[u^{(k)}_{\phi,\phi}\right]^{*}\left[F^{(l)}\right]^{*}\eta^{(p)}_{ri,r}-\left[u^{(k)}_{r,r}\right]^{*}\left[F^{(l)}\right]^{*}\eta^{(p)}_{\theta i,\theta}\\
&-\left[u^{(k)}_{\theta,\theta}\right]^{*}\left[F^{(l)}\right]^{*}\eta^{(p)}_{ri,r}-\left[u^{(k)}_{r,r}\right]^{*}\left[F^{(l)}\right]^{*}\eta^{(p)}_{\phi i,\phi}-\left[u^{(k)}_{\phi,\phi}\right]^{*}\left[H^{(l)}\right]^{*}\eta^{(p)}_{\theta i,\theta}\\
&-\left[u^{(k)}_{\theta,\phi}\right]^{*}\left[N^{(l)}\right]^{*}\eta^{(p)}_{\theta i,\phi}-\left[u^{(k)}_{\theta,\phi}\right]^{*}\left[N^{(l)}\right]^{*}\eta^{(p)}_{\phi i,\theta}-\left[u^{(k)}_{\phi,\theta}\right]^{*}\left[N^{(l)}\right]^{*}\eta^{(p)}_{\theta i,\phi}-\left[u^{(k)}_{\phi,\theta}\right]^{*}\left[N^{(l)}\right]^{*}\eta^{(p)}_{\phi i,\theta}\\
&-\left[u^{(k)}_{\phi,r}\right]^{*}\left[L^{(l)}\right]^{*}\eta^{(p)}_{\phi i,r}-\left[u^{(k)}_{\phi,r}\right]^{*}\left[L^{(l)}\right]^{*}\eta^{(p)}_{ri,\phi}-\left[u^{(k)}_{r,\phi}\right]^{*}\left[L^{(l)}\right]^{*}\eta^{(p)}_{\phi i,r}-\left[u^{(k)}_{r,\phi}\right]^{*}\left[L^{(l)}\right]^{*}\eta^{(p)}_{ri,\phi}\\
&-\left[u^{(k)}_{r,\theta}\right]^{*}\left[L^{(l)}\right]^{*}\eta^{(p)}_{ri,\theta}-\left[u^{(k)}_{r,\theta}\right]^{*}\left[L^{(l)}\right]^{*}\eta^{(p)}_{\theta i,r}-\left[u^{(k)}_{\theta,r}\right]^{*}\left[L^{(l)}\right]^{*}\eta^{(p)}_{ri,\theta}-\left[u^{(k)}_{\theta,r}\right]^{*}\left[L^{(l)}\right]^{*}\eta^{(p)}_{\theta i,r}.
\end{aligned}
\tag{A2}
$$

[49] **Acknowledgments.** We thank Kei Hirose, Shigenori Maruyama, Taku Tsuchiya, and Nozomu Takeuchi for valuable discussions. Data were obtained from IRIS and BDSN data servers. This research was partly supported by grants from the Japanese Ministry of Education, Science and Culture (19740272) and a JSPS Fellowship for Young Scientists to K.K.

References

Akaike, H. (1977), An extension of the method of maximum likelihood and the Stein's problem, *Ann. Inst. Stat. Math.*, *29*, 153–164.

Avants, M., T. Lay, and E. J. Garnero (2006a), A new probe of ULVZ *S* wave velocity structure: Array stacking of *ScS* waveforms, *Geophys. Res. Lett.*, *33*, L07314, doi:10.1029/2005GL024989.

Avants, M., T. Lay, S. A. Russell, and E. J. Garnero (2006b), Shear velocity variation within the D″ region beneath the central Pacific, *J. Geophys. Res.*, *111*, B05305, doi:10.1029/2004JB003270.

Christensen, U. R., and A. W. Hofmann (1994), Segregation of subducted oceanic-crust in the convecting mantle, *J. Geophys. Res.*, *99*, 19,867–19,884.

Dziewonski, A. M., and D. L. Anderson (1981), Preliminary reference Earth model, *Phys. Earth Planet. Inter.*, *25*, 297–356.

Geller, R. J., and T. Hara (1993), Two efficient algorithms for iterative linearized inversion of seismic waveform data, *Geophys. J. Int.*, *115*, 699–710.

Geller, R. J., and T. Ohminato (1994), Computation of synthetic seismograms and their partial derivatives for heterogeneous media with arbitrary natural boundary conditions using the direct solution method, *Geophys. J. Int.*, *116*, 421–446.

Geller, R. J., and N. Takeuchi (1995), A new method for computing highly accurate DSM synthetic seismograms, *Geophys. J. Int.*, *123*, 449–470.

Grand, S. P. (2002), Mantle shear wave tomography and the fate of subducted slabs, *Philos. Trans. R. Soc., Ser. A*, *360*, 2475–2491.

Grand, S. P., and D. V. Helmberger (1984), Upper mantle structure shear structure of North America, *Geophys. J. R. Astron. Soc.*, *76*, 399–438.

Hara, T. (2004), Waveform inversion for 3-D earth structure using the direct solution method implemented on vector-parallel supercomputer, *Phys. Earth Planet. Inter.*, *146*, 65–74.

Hara, T., and R. J. Geller (2000), Simultaneous waveform inversion for 3-D Earth structure and earthquake source parameters considering a wide range of modal coupling, *Geophys. J. Int.*, *142*, 539–550.

Hernlund, J. W., C. Thomas, and P. J. Tackley (2005), A doubling of the post-perovskite phase boundary and structure of the Earth's lowermost mantle, *Nature*, *434*, 882–886.

Karki, B. B., L. Stixrude, and J. Crain (1997), Ab initio elasticity of three high-pressure polymorphs of silica, *Geophys. Res. Lett.*, *24*, 3269–3272.

Kawai, K., and T. Tsuchiya (2009), Temperature profile in the lowermost mantle from seismological and mineral physics joint modeling, *Proc. Natl. Acad. Sci. U. S. A.*, *106*, 22,119–22,123, doi:10.1073/pnas.0905920106.

Kawai, K., N. Takeuchi, and R. J. Geller (2006), Complete synthetic seismograms up to 2 Hz for transversely isotropic spherically symmetric media, *Geophys. J. Int.*, *164*, 411–424.

Kawai, K., N. Takeuchi, R. J. Geller, and N. Fuji (2007a), Possible evidence for a double crossing phase transition in D″ beneath Central America from inversion of seismic waveforms, *Geophys. Res. Lett.*, *34*, L09314, doi:10.1029/2007GL029642.

Kawai, K., R. J. Geller, and N. Fuji (2007b), D″ beneath the Arctic from inversion of shear waveforms, *Geophys. Res. Lett.*, *34*, L21305, doi:10.1029/2007GL031517.

Kawai, K., S. Sekine, N. Fuji, and R. J. Geller (2009), Waveform inversion for D″ structure beneath northern Asia using Hi-net tiltmeter data, *Geophys. Res. Lett.*, *36*, L20314, doi:10.1029/2009GL039651.

Konishi, K., K. Kawai, R. J. Geller, and N. Fuji (2009), MORB in the lowermost mantle beneath the western Pacific: Evidence from waveform inversion, *Earth Planet. Sci. Lett.*, *278*, 219–225.

Lay, T., and D. V. Helmberger (1983), A lower mantle *S* wave triplication and the shear velocity structure of D″, *Geophys. J. R. Astron. Soc.*, *75*, 799–838.

Lay, T., J. W. Hernlund, E. J. Garnero, and M. S. Thorne (2006), A post-perovskite lens and D″ heat flux beneath the central Pacific, *Science*, *314*, 1272–1276.

Li, X. D., and B. Romanowicz (1995), Comparison of global waveform inversions with and without considering cross-branch modal coupling, *Geophys. J. Int.*, *121*, 695–709.

Li, X. D., and B. Romanowicz (1996), Global mantle shear velocity model developed using nonlinear asymptotic coupling theory, *J. Geophys. Res.*, *101*, 22,245–22,272.

Love, A. E. H. (1927), *A Treatise on the Mathematical Theory of Elasticity*, Cambridge Univ. Press, Cambridge, U. K.

Maruyama, S., M. Santosh, and D. P. Zhao (2007), Superplume, supercontinent, and post-perovskite: Mantle dynamics and anti-plate tectonics on the core-mantle boundary, *Gondowana Res.*, *11*, 7–37.

McDonough, W. F., and S. Sun (1995), The composition of the Earth, *Chem. Geol.*, *120*, 223–253.

Megnin, C., and B. Romanowicz (2000), The three-dimensional shear velocity structure of the mantle from the inversion of body, surface and higher-mode waveforms, *Geophys. J. Int.*, *143*, 709–728.

Montagner, J. P. (1986), Regional three-dimensional structures using long-period surface waves, *Ann. Geophys., Ser. B*, *4*, 283–294.

Murakami, M., K. Hirose, K. Kawamura, N. Sata, and Y. Ohishi (2004), Post-perovskite phase transition in $MgSiO_3$, *Science*, *304*, 855–858.

Nolet, G. (1990), Patitioned waveform inversion and two-dimensional structure under the Network of Autonomously Recording Seismographs, *J. Geophys. Res.*, *95*, 8499–8512.

Ohta, K., K. Hirose, T. Lay, N. Sata, and Y. Ohishi (2008), Phase transitions in pyrolite and MORB at lowermost mantle conditions: Implications for a MORB-rich pile above the core-mantle boundary, *Earth Planet. Sci. Lett.*, *267*, 107–117.

Ringwood, A. E. (1962), A model for the upper mantle, *J. Geophys. Res.*, *67*, 857–867.

Ritsema, J., E. J. Garnero, and T. Lay (1997), A strongly negative shear velocity gradient and lateral variability in the lowermost mantle beneath the Pacific, *J. Geophys. Res.*, *102*, 20,395–20,411.

Suetsugu, D., et al. (2005), Mantle discontinuity depths beneath the West Philippine Basin from receiver function analysis of deep-sea borehole and seafloor broadband waveforms, *Bull. Seismol. Soc. Am.*, *95*, 1947–1956.

Sutherland, F. H., F. L. Vernon, J. A. Orcutt, J. A. Collins, and R. A. Stephen (2004), Results from OSNPE: Improved teleseismic earthquake detection at the seafloor, *Bull. Seismol. Soc. Am.*, *94*, 1868–1878.

Tackley, P. J. (2000), Mantle convection and plate tectonics: Toward an integrated physical and chemical theory, *Science*, *288*, 2002–2007.

Tajima, F., and S. P. Grand (1998), Variation of transition zone high-velocity anomalies and depression of 660 km discontinuity associated with subduction zones from the southern Kuriles to Izu-Bonin and Ryukyu, *J. Geophys. Res.*, *103*, 15,015–15,036.

Takeuchi, N. (2007), Whole mantle SH velocity model constrained by waveform inversion based on three-dimensional Born kernels, *Geophys. J. Int.*, *169*, 1153–1163.

Tsuchiya, J., and T. Tsuchiya (2008), Postperovskite phase equilibria in the $MgSiO_3$-Al_2O_3 system, *Proc. Natl. Acad. Sci. U. S. A.*, *105*, 19,160–19,164.

Tsuchiya, T., and J. Tsuchiya (2006), Effect of impurity on the elasticity of perovskite and postperovskite: Velocity contrast across the postperovskite transition in $(Mg,Fe,Al)(Si,Al)O_3$, *Geophys. Res. Lett.*, *33*, L12S04, doi:10.1029/2006GL025706.

Tsuchiya, T., J. Tsuchiya, K. Umemoto, and R. A. Wentzcovitch (2004), Phase transition in $MgSiO_3$ perovskite in the Earth's lower mantle, *Earth Planet. Sci. Lett.*, *224*, 241–248.

Wiggins, R. A. (1972), The general linear inverse problem implication of surface waves and free oscillation for Earth structure, *Rev. Geophys. Space Phys.*, *10*, 251–285.

Woodhouse, J. H., and A. M. Dziewonski (1984), Mapping the upper mantle: Three-dimensional modeling of Earth structure by inversion of seismic waveforms, *J. Geophys. Res.*, *89*, 5953–5986.

R. J. Geller, Department of Earth and Planetary Science, Graduate School of Science, University of Tokyo, Hongo 7-3-1, Bunkyo-ku, Tokyo, 113-0033, Japan. (bob@eps.s.u-tokyo.ac.jp)

K. Kawai, Department of Earth and Planetary Sciences, Tokyo Institute of Technology, Ookayama 2-12-1, Meguro-ku, Tokyo, 152-8551, Japan. (kenji@geo.titech.ac.jp)